1-1-2014

Characteristics of oxide scale formed on ferritic stainless steels in simulated reheating atmosphere

Xiawei Cheng
University of Wollongong, xc979@uowmail.edu.au

Zhengyi Jiang
University of Wollongong, jiang@uow.edu.au

Dongbin Wei
University of Technology, Sydney, dwei@uow.edu.au

Jingwei Zhao
University of Wollongong, jzhao@uow.edu.au

Brian J. Monaghan
University of Wollongong, monaghan@uow.edu.au

See next page for additional authors

Characteristics of oxide scale formed on ferritic stainless steels in simulated reheating atmosphere

Abstract

The aim of this study is to optimise the stainless steel oxidation behaviours during hot rolling. The high temperature oxidation behaviours of ferritic stainless steels B443NT and B445J1M were studied over the temperature range from 1000 to 1150 °C in a humid atmosphere containing 18% water vapour, as measured by a thermogravimetric analyser (TGA). The results indicate that breakaway oxidation occurs at 1090 °C for the B443NT steel, which is 60 °C lower than that for the B445J1M steel. The occurrence of iron oxide nodules on the steels marks the onset of breakaway oxidation; however, the breakaway oxidation phenomenon of B445J1M is different from that of B443NT due to a compact and continuous Mn-Cr spinel which is formed on the surface of B445J1M. The oxide nodules with regenerated Cr2O3 scale underneath the Fe-Cr spinel display better adhesion without showing pores at the metal-scale interface.

Disciplines

Engineering | Science and Technology Studies

Publication Details

Cheng, X., Jiang, Z., Wei, D., Zhao, J., Monaghan, B. J., Longbottom, R. J. & Jiang, L. (2014). Characteristics of oxide scale formed on ferritic stainless steels in simulated reheating atmosphere. Surface and Coatings Technology, 258 257-267.

Authors

Xiawei Cheng, Zhengyi Jiang, Dongbin Wei, Jingwei Zhao, Brian J. Monaghan, Raymond J. Longbottom, and Laizhu Jiang

Characteristics of oxide scale formed on ferritic stainless steels in simulated reheating atmosphere

Xiawei Cheng[1], Zhengyi Jiang[1,*], Dongbin Wei[2], Jingwei Zhao[1], Brian J. Monaghan[1], Raymond J. Longbottom[1], Laizhu Jiang[3]

[1]School of Mechanical, Materials and Mechatronic Engineering, University of Wollongong, NSW 2522, Australia
[2]School of Electrical, Mechanical and Mechatronic Systems, University of Technology Sydney, NSW 2007, Australia
[3]Baosteel Research Institute (R&D Centre), Baoshan Iron & Steel Co., Ltd., Shanghai 200431, PR China

Abstract

The aim of this study is to optimise the stainless steel oxidation behaviours during hot rolling. High temperature oxidation behaviours of ferritic stainless steels B443NT and B445J1M were studied over the temperature range from 1000 to 1150 °C in humid atmosphere containing 18% water vapour by thermogravimetric analyser (TGA). The results indicate that the breakaway oxidation occurs at 1090 °C for the B443NT steel, which is 60 °C lower than that for the B445J1M steel. The occurrence of iron oxide nodules on the steels marks the onset of breakaway oxidation; however, the breakaway oxidation phenomenon of B445J1M is different from that of B443NT due to a compact and continuous Mn-Cr spinel formed on the surface of B445J1M. The oxide nodules with regenerated Cr_2O_3 scale underneath the Fe-Cr spinel display better adhesion without showing pores at the metal-scale interface.

Keywords: Ferritic stainless steel; High temperature oxidation; Water vapour; Oxide scale

* Corresponding author. Tel: +61-2-42214774; Fax: +61-2-42215474
E-mail addresses: xc979@uowmail.edu.au (X. Cheng), jiang@uow.edu.au (Z. Jiang), jwzhaocn@gmail.com (J. Zhao)

1. Introduction

Ferritic stainless steels containing little or no nickel are widely used because of their excellent resistance to oxidation and corrosion, and as well as lower price. Ferritic stainless steels have a lower thermal expansion coefficient than that of austenitic steels [1], which is clearly an advantage when the temperature cycling resistance is needed. For instance, ferritic stainless steels exhaust catalysis units for automobiles. However, oxide scale is hard to be formed on the surface of stainless steels relative to carbon steels at processing (e.g. hot rolling) temperatures because of their excellent oxidation resistance. Sticking problem between the rolls and strips will occur due to the lack of oxide scale protection in the hot rolling of stainless steel strips, and a decreased surface quality of the final products will be caused [2]. Sticking refers to a phenomenon occurring in the hot rolling process in which fragments of a rolled material are detached and get stuck to a work roll surface, deteriorating the surfaces of both the rolls and the rolled material. With the development of new ferritic stainless steels with a high amount of Cr, it is necessary to understand the oxidisation characteristics of such ferritic stainless steels in the reheating environment.

In the reheating furnace, the temperature can be as high as 1200 °C. The atmosphere in such furnace generally contains moisture due to the natural gas combustion and/or humid conditions. The effect of water vapour on the stainless steel oxidation has already been described in the literature [3-7]. Douglass et al. [8] stated that the water vapour had a major effect on the oxidation rate of chromia-forming alloys and that this was most marked for iron-based alloys. Generally, the exposure of Fe-Cr alloys to O_2/H_2O mixtures at the temperatures above 500°C results in a degradation of Cr oxide by the evapouration of Cr species $CrO_2(OH)_2$ or CrO_3 [9]. The evapouration rate of Cr_2O_3 is linearly dependent on time in N_2-O_2-H_2O atmospheres, and a higher temperature results in a higher evapouration rate [10]. Chromium evaporation can lead to its depletion from the protective oxide scale [11], resulting

in the formation of poorly protective Fe-rich oxide scale and thus an increased oxidation rate. The faster oxidation rates were attributed to lower Cr/Fe ratios in the scales, and consequently higher solid-state diffusion rates [12].

Long-term oxidation behaviour of some ferritic stainless steels has been intensively studied due to their applications to solid oxide fuel cells (SOFC) stack [13-15]. However, the operation temperature for these studies is always lower than 1000 °C and it is not related to the reheating environment. Steel grades B443NT and B445J1M, new ferritic stainless steels developed by Baosteel, China, were found to have severe sticking phenomenon during hot rolling. In order to understand well the mechanism of surface deterioration and reduce the occurrence of sticking of stainless steel strips during hot rolling, a fundamental research is necessary to clearly understand the mechanism of oxide scale formation on the strip surface and develop effective control strategies for optimising the oxide scale structures. Significant benefit will be satisfied in the form of product quality improvement and production cost reduction.

The objective of this study is to investigate the characteristics of oxide scale formed on the surfaces of two stainless steels grads B443NT and B445J1M over the temperature range from 1000 to 1150 °C in a simulated reheating atmosphere with 18% water vapour. Oxidation kinetics, and as well as the evolution of oxide scale composition and microstructure are systematically studied. The mechanism of the formation of oxide scale on both steels is discussed. The research has practical applications, and the outcomes will be helpful in the design of hot rolling processes of these stainless steels.

2. Experimental method

2.1. Materials

Two ferritic stainless steels, B443NT and B445J1M, were used in this study. The chemical compositions of the steels are given in Table 1. Samples with size of 20 mm × 10 mm × 1 mm were machined from a hot-rolled slab with a small hole of 2 mm in diameter near an edge. Prior to the oxidation experiments, all the samples were ground on all sides with 1200 grit SiC sandpaper, then cleaned in acetone and rinsed with alcohol.

2.2. Oxidation experiments

The oxidation kinetics of stainless steels was investigated using a thermogravimetric analyser (TGA). Oxidation tests were performed in an apparatus shown in Fig. 1. Before the tests, temperature calibration was carried out at the test temperatures. Samples were put in a vertical tube furnace and isothermally heated for 120 min, which is consistent with the real time of reheating. The mass change of a sample during TGA experiment was measured using a Sartorius CP124S microbalance with a resolution of 10^{-4} g, and the value was recorded automatically by a connected computer. A simulated humid atmosphere with 18% water vapour was generated by water bath and flowed into the furnace at a rate of 1000 ml/min by bubbling synthetic air through the water bath with the water temperature of 58.4 °C. The gas inlet line was heated to prevent water vapour condensation. The total gas pressure was 1 atm.

The furnace was heated to the set temperature at a heating rate of 20 °C/min, then humid air flowed through the furnace. The furnace was held at the set temperature for 30 min, then the steel sample was lowerered into the hot zone of the furnace and the weight change logged. After the set time of 120 min, the experiment was ended by removing the sample from the furnace and cooling it in air to room temperature.

2.3. Analysis of oxide scale

Surface 3D profiles of the oxide scales formed on samples were examined by a VHX-1000E

Digital Microscope. After surface analysis, all the samples were cold mounted in epoxy resin, then sectioned and polished. The microstructures, compositions and thickness of the oxide scale were examined by a JEOL JSM 6490 scanning electron microscope (SEM) equipped with an Energy Dispersive Spectrometer (EDS). Oxide scales formed on the samples were surface scanned using X-ray diffraction (XRD) for the phase identification.

3. Results

3.1. Oxidation kinetics

Fig. 2a and b present the variations of mass gain with time for the B443NT and B445J1M stainless steels oxidised from 1000 to 1150 °C in a humid atmosphere with 18% water vapour, respectively. As shown in Fig. 2a, the curves of the B443NT steel present a parabolic law tendency from 1000 to 1060 °C and the mass gains at 120 min are 1.02, 1.21 and 1.40 $mg \cdot cm^{-2}$, respectively. At 1090 °C and 1120 °C, the oxidation rates have an abrupt increase indicating the occurrence of breakaway oxidation, after which the oxidation follows a linear law. At 1150 °C, the high oxidation rate is achieved within 10 min, following a linear law and then a parabolic regime. The curves of B445J1M also present a parabolic law from 1000 to 1120 °C, as shown in Fig. 2b. The oxidation rates of B445J1M during the parabolic regime are slightly higher compared to those of B443NT from 1000 to 1060 °C. At 1150 °C an abrupt increase of oxidation rate is observed within 10 min, after which a parabolic law is followed.

Compliance to the parabolic law indicates that the reaction is of a diffusion-controlled character at all temperatures [16]. High temperature oxidation kinetics of metals or alloys is commonly controlled by the diffusion of cationic or anionic species through the oxide scale [17]. Such a control leads to a parabolic rate constant, K_p, expressed in $mg^2 \cdot cm^{-4} \cdot s^{-1}$, and defined by [17]:

$$(\Delta m/s)^2 = A + K_p t \quad (1)$$

where $\Delta m/s$ is the specific mass gain per area unit in mg/cm^2, t is the oxidation time, and A is a constant. The regressed parabolic rate constants for the steel B445J1M oxidised at different temperatures in humid atmosphere are given in Table 2. In Table 2, the multiple coefficient of determination R^2 is a measure of the loss of predictive power or shrinkage in regression. R^2 explains how much variance in the outcome would be accounted for if the model has been derived from the variables from which the sample was taken. The larger value of R^2, the better the model fits the data. K_p values and associated R^2 values have been calculated for fits of equation 1 to the data in Fig. 2b for the steel B445J1M. There was little weight gain in samples of this steel, particularly at the lower temperatures. This increases the uncertainty in the K_p values calculated for this steel. It is evident in the lower R^2 value obtained for experiments at the temperature <= 1060°C. Given this it is difficult to distinguish the effects of temperature on the rate of oxidation below this temperature. All that can reasonably be stated is that the K_p (and oxidation rate) is small and broadly consistent with parabolic oxidation kinetics.

3.2. Oxide scale phase identities

A conventional diffraction meter operating with Cu K_α radiation was used for X-ray analysis by applying the step method with a constant counting time per step. The step method involves 0.02° steps and counting time of 4 s at each step. Fig. 3a and b show the XRD patterns of the oxide scale formed on the B443NT and B445J1M steels oxidised at different temperatures in humid atmosphere containing 18% water vapour, respectively. XRD analysis reveals that the compositions of oxide scales on the two steel grades are Cr_2O_3 and spinel M_3O_4. M might be Cr, Mn, and/or Fe because of the similar ionic radii of Cr, Mn, and Fe [18]. Therefore, it is difficult to determine the exact composition of the spinel by the positions of the spinel peaks in the XRD pattern. On the other hand, the spinels on the B445J1M steel are more likely $Mn_{1.5}Cr_{1.5}O_4$ or $MnCr_2O_4$. Mn-Cr spinel on the B445J1M steel may not have stoichiometric

compositions as diffraction peaks shift slightly to the lower angle. With the aid of EDS spot, line and map element analysis on the cross section of the oxide scale, the composition of the spinel could be identified and will be detailed in the following Section 3.3. The oxide scale on the B443NT steel oxidised at 1000 °C is so thin that the substrate Fe-Cr is detected by XRD. As the temperature is increased to 1150 °C, only one phase, Fe_2O_3 is detected due to the thick oxide scale and the ray of XRD cannot penetrate deeply to detect other phases underneath.

3.3. Oxide scale surface and cross section morphology

The oxide scale surface and cross section morphology were analysed for the samples that were oxidised for 120 min after they were cooled down.

The SEM micrographs of the surface of oxide scale formed on the B443NT steel at different temperatures oxidised for 120 min in humid atmosphere with 18% water vapour are shown in Fig. 4a-d.

The oxide scale formed at 1000 °C and 1030 °C as shown in Fig. 4a and b, has a homogeneous microstructure. Some coarse hexagonal spinel crystallites are embedded in the fine chromia scale matrix. Oxide spallation was observed on the specimen oxidised at 1000 °C, as shown in Fig. 4a, and on the steel matrix some imprints were left due to the spallation. The oxide scale formed at 1090 °C, as shown in Fig. 4c, is significantly different from that grown at lower temperatures. Localised iron rich oxide nodules extrude above the surface, exhibiting a coarse surface. The edges of the specimens were totally covered with iron rich oxides. The iron rich nodules, once formed, result in large mass gain, accelerated oxide scale growth, and breakaway oxidation. As the temperature reaches 1150 °C, as shown in Fig. 4d, the iron rich nodules merge, therefore, nearly all the surface is covered with hematite. The oxide scale growth rate is significantly high compared to the lower temperatures. However,

there are still some small regions having a thin oxide scale.

SEM and EDS analysis on the cross sections of B443NT oxidised from 1000 to 1060 °C, as shown in Fig. 5a-c, reveal the void/gap between the steel substrate and the oxide scale, especially at 1000 °C, some oxide scale is totally detached from the steel substrate, indicating that the oxide scale has the weak adhesion to steel substrate. However, the oxide scale is pined by the steel substrate along the metal-scale interface, as shown in Fig. 5b and c. EDS line scanning analysis across the interface of the steel substrate and the oxide scale were performed. Cr is dominant in the oxide scale, indicating the main composition is Cr_2O_3. The intensity of Si at the metal-scale interface increases with increasing the temperature. However, the silica layer beneath Cr_2O_3 is porous. Mn distributes almost evenly across the oxide scale, only slightly more on the surface at 1000 and 1030 °C. Ti segregates in the steel substrate close to the metal-scale interface.

The SEM image and EDS element maps of the cross section of the specimen oxidised at 1090 °C with nodules are shown in Fig. 6. Si is still present with Cr, displaying the position of original metal-scale interface. It indicates that Si hardly diffuses in iron oxides. On the surface where the nodules are formed, iron rich oxides grow outwards and Fe-Cr spinel grows inwards, penetrating into the substrate and consuming of metal elements, resulting in local metal loss or attack.

EDS element map of the cross section of the specimen oxidised at 1150 °C with small region of the thin oxide scale is shown in Fig. 7. Si is present at the original metal-scale interface of which is now the interface between iron oxide and Fe-Cr spinel. In addition, Si is present with Cr rich region in the spinel where the metal-scale interface is. Mn is present most at where used to be Cr_2O_3 before breakaway oxidation occurs.

The SEM micrographs of the surface of oxide scale formed on the B445J1M steel at different temperatures oxidised for 120 min in humid atmosphere with 18% water vapour are shown in Fig. 8a-d.

The oxide scale formed at 1000 °C, as shown in Fig. 8a, has a homogeneous microstructure. The similar surface morphology is at 1030 and 1060 °C. EDS analysis of the bright phases on the surface shows that they are rich in Cr. Spinel crystallites are embedded in the matrix of Cr_2O_3. Mn is abundant in the structure of the spinel, matching $(Mn,Cr)_3O_4$ by XRD analysis. Fig. 8b shows that the surface of the oxide scale formed at 1090 °C is bulky, but the oxide grains are still small with some spinel crystallites.

For the oxide scale formed at 1120 °C, sparse small oxide nodules appear, as shown in Fig. 8c, where they are formed mostly on the bulky surface. EDS analysis of the nodule surface shows the oxide nodules are still rich in Cr. however; the oxide scale formed at 1150 °C, as shown in Fig. 8d is different from that formed at lower temperatures. It is like that formed at 1090 °C on B443NT. That is, localised iron rich nodules appear and grow laterally with a coarse surface, marking the occurrence of breakaway oxidation. It can be seen from Fig. 8e and f, the surface is rougher at 1150 °C than that at 1120 °C.

SEM and EDS analysis was performed on the cross sections of B445J1M oxidised from 1030 to 1120 °C, as shown in Fig. 9a-d. The morphology of the cross section of the oxide scale is quite similar to that formed on B443NT. Si segregates at the metal-scale interface, and as well the silica layer is porous. The intensity of Si at the metal-scale interface increases with increasing the temperature. The oxide scale is pined by the steel substrate along the metal-scale interface. Cr is dominant in the oxide scale, indicating the main composition is Cr_2O_3.

Mn distributes across the oxide scale, slightly more on the surface from 1030 to 1060 °C, but showing the high intensity at the temperatures of 1090 and 1120 °C. Ti segregates in the steel substrate close to the metal-scale interface.

The SEM image and EDS element map of the cross section of the specimen oxidised at 1150 °C with nodules is shown in Fig. 10. A strong indication of Cr is present at the metal-scale interface, along with Si. Iron oxides grow outwards and Fe-Cr spinel grows inwards by consuming the metal substrate.

The morphology and EDS line scanning analysis of the interface of the metal-scale where the oxide nodules were formed on B443NT and B445J1M at 1150 °C are shown in Fig. 11a and b. Fig. 11a shows that voids exist at the interface, and the internal Cr rich oxide forms in the steel substrate. Cr depletion is detected underneath the oxide scale in a range of 10 μm. The Cr content on B443NT near the metal-oxide interface is about 11.2 wt.% (location A). Fig. 11b shows that the oxide scale close to the metal-scale interface is compact. The small black islands underneath the oxide scale are enriched in Si. Moreover, in the oxide scale just above the interface of metal-scale, the intensity of Fe is negligible and Cr is high, illustrating that a healing film of Cr_2O_3 is regenerated, which can prevent the Fe-Cr spinel from growing deep into the substrate. The Cr content on B445J1M near the metal-oxide interface is about 19.6 wt.% (location B), indicating no obvious Cr depletion occurs. On the other hand, no large cavities can be seen at the metal-scale interface, showing that the oxide scale is adherent to the substrate.

4. Discussion

Both the studied stainless steels B443NT and B445J1M have very good oxidation resistance at high temperatures. However, in the humid atmosphere used B445J1M steel can tolerate

higher temperatures than B433NT steel before breakaway oxidation occurs. Before the breakaway oxidation happens, the oxide scale is mainly constituted of Cr_2O_3, as shown in Figs. 5 and 9. Kinetics results obtained during high temperature oxidation of B445J1M are reported in Table 2. The Arrhenius plot of oxidation parabolic constants determined from four measurements from temperatures 1030 to 1120 °C is shown in Fig. 12a. The activation energy value is obtained to be 263 kJ/mol for the oxidation reaction of B445J1M before the breakaway oxidation occurs. The result agrees well with the formation of protective chromia film [19-21]. The breakaway oxidation phenomenon of B445J1M is different from that of B443NT (Fig. 2), which shows an abrupt increase of oxide scale growth rate when the chromia transits to iron oxides. The parabolic nature of the breakaway oxidation for the two stainless steels at 1150 °C can be established in Fig 12b, which is the graph of mass gain against square root of oxidation time. The parabolic growth rate constant K_p of B443NT is 6.3×10^{-1} $mg^2 \cdot cm^{-4} \cdot s^{-1}$, and for B445J1M, a lower calculated K_p value, 3.0×10^{-3} $mg^2 \cdot cm^{-4} \cdot s^{-1}$ is derived. However, the iron oxide was developed at this stage (Fig. 4d). The slower oxide growth rate may be attributed by the regeneration of Cr_2O_3 underneath the iron oxide (Fig. 10).

The present study shows the thinned Cr_2O_3 oxide scale formed on B443NT as compared to B445J1M at the same testing temperature. Based on the TGA results, the mass gain of the B443NT steel is lower than that of the B445J1M steel at the temperatures from 1000 to 1060 °C, indicating thinner oxide scale formed on the B443NT steel relative to that on the B445J1M steel. Fig. 13a and b show the cross section of the thin oxide scale formed on B443NT and B445J1M at 1150 °C for 120 min, where the iron oxides have not grown on. It can be seen from Fig. 13b that continuous and compact external Mn-Cr spinel layer is formed on B445J1M but no spinel layer formed on the top of Cr_2O_3 on B443NT. On the other hand, the oxide scale on B445J1M is thicker than that on B443NT. Pores, gaps and cracks are found

at the metal-scale interface of the two steels.

In the case of B443NT, the breakaway oxidation occurs at relatively low temperature and a high growth rate is followed. This is caused by the Cr depletion in the subscale zone by selective oxidation of Cr [16, 22]. Generally, the greater the extent of the Cr depletion, the less likely it will be for the Cr_2O_3 scale to be healed or reformed [23-24]. Before the breakaway oxidation occurs, a continuous external Cr_2O_3 scale forms on the two steels (Figs. 5 and 9). In order to develop and maintain the Cr_2O_3 scale, the interfacial concentration of Cr, $N_{Cr}^{(i)}$, is determined by the rates at which Cr is being consumed by the Cr_2O_3 scale growth and replenished by Cr diffusion in the alloy. Wagner's diffusion analysis [25] leads to an expression as [26]:

$$N_{Cr}^{(0)}\text{-}N_{Cr}^{(i)}=\frac{V_A}{V_{CrO_{1.5}}}\left(\frac{\pi k_c}{2\widetilde{D}}\right)^{1/2} \quad (2)$$

where $N_{Cr}^{(0)}$is the original alloy chromium concentration, V_A and $V_{CrO_{1.5}}$ are respectively the molar volumes of alloy and oxide scale, $\widetilde{D}$ is the alloy interdiffusion coefficient, and K_c is the parabolic rate constant for growth of the external scale which is measured in term of oxide scale thickness. K_c can also be calculated from K_p, the parabolic rate constant from mass gain, using for an oxide film M_aO_b, which can be expressed as [17].

$$K_c=\left(\frac{\Delta M\times M_{ox}}{SbM_o\rho_{ox}}\right)^2 K_p \quad (3)$$

where ΔM is the mass gain, S is the surface area, M_{ox} is the molar mass of the oxide, M_o is the molar mass of the oxygen atom, ρ_{ox} is the volumic mass of the oxide.

The two ferritc stainless steels have roughly the same steel structure and similar content of Cr. The parameters V_A, $V_{CrO_{1.5}}$ and $\widetilde{D}$ are nearly same. Slightly higher content of Cr in B445J1M leads to a higher value of $N_{Cr}^{(0)}$, however, its K_c is higher than that of B443NT, then results in

no much difference of $N_{Cr}^{(i)}$ between B443NT and B445J1M. It is concluded that the growth of the Cr_2O_3 scale is not the reason to cause the depletion of Cr in B443NT. Moreover, from the experimental results, it is clear that Cr is well preserved in B445J1M, even at the high temperature of 1150 °C, the regeneration of Cr_2O_3 underneath the Fe-Cr oxides takes place (Fig. 11b). The effects of water vapour and temperature on all of these processes need to be considered.

Several authors [12, 26-29] attributed the loss of protection of chromia-base surface scales to the enhanced formation of volatile Cr oxy-hydroxide, $CrO_2(OH)_2$ via the following reaction:

$$1/2Cr_2O_3\ (s) + H_2O\ (g) + 3/4O_2\ (g) = CrO_2\ (OH)_2\ (g) \quad (4)$$

Then, the equilibrium partial pressure of the volatile oxy-hydroxide is given by

$$P_{CrO_2(OH)_2} = KP_{H_2O} \cdot P_{O_2}^{3/4} \quad (5)$$

where K is given by [30].

$$\ln(K) = -6435/T - 5.473 \quad (6)$$

The present study was carried out in humid air with 18% water vapour at 1 atm. The partial pressure for O_2 and H_2O is 0.164 and 0.18 atm, respectively, and the value of K is bigger at the higher temperature, therefore the volatile Cr species will form at such an atmosphere. Yamauchi et al. [10] also found that the deterioration of Cr_2O_3 scale is likely to occur in mixed atmospheres of oxygen and water vapour. The thinning of Cr_2O_3 scale will increase the Cr depletion and the oxidation rate of the alloys. However, this is not applicable to B445J1M due to a continuous and compact $(Mn,Cr)_3O_4$ spinel layer formed on the top of the Cr_2O_3 scale (Figs. 9d, e and 13b). Holcomb et al. [31] proposed that $MnCr_2O_4$ strongly reduced $CrO_2(OH)_2$ volatilisation when presented at the external interface.

Our study shows that Mn plays a significant role in the high temperature oxidation behaviour. The amount of Mn in the B445J1M steel is higher than that in the B443NT steel. It shows that the amount of Mn on the top of the oxide film is limited by the small amount of Mn in the steel. Mn content in the oxides layers is found to coexist with the Cr oxide (Figs. 6 and 10), demonstrating that Mn has a higher affinity to oxygen than iron and a greater diffusivity through the Cr oxide [32]. For the oxides formed on the B445J1M steel, Mn is rich at the gas-scale interface, and spinel $(Mn,Cr)_3O_4$ is detected. The formation of Mn-Cr oxide can reduce Cr activity, and Mn-Cr oxides are known to provide protection against oxidation [33-34]. Sabioni et al. [35] have investigated the presence of Mn on chromia forming alloy. Their study showed that Mn-rich particles on the outer surface resulted from the initial oxidation, due to the fact that Mn affinitiy for O_2 is greater than Cr affinity, with the process of time, Mn ion will diffusion through chromia towards the outer surface of the oxide scale. With stainless steel 430 alloys containing various contents of Mn (0.1-0.9 wt.%) oxidised at 1000°C in 0.165 atm O_2-N_2 atmosphere, Saeki et al. [24] found that corundum type oxide scale formed within first 30 s followed by formation of spinel type oxide scale nucleated from the pre-existing corundum oxides. At a lower oxidation temperature, Mn diffusion rate in Fe-Cr alloy may not be as high as that at high temperatures. Issartel et al. [36] carried out in-situ XRD analyses for the steel with a Mn content of 0.45 wt.%. $Mn_{1.5}Cr_{1.5}O_4$ spinel was found to appear after 13 h at 800 °C in air. However, with further increase of Mn content, Mn-rich oxides such as Mn_2O_3 and Mn_3O_4 will form on the outermost surface of Fe–Cr alloys, resulting in a higher oxidation rate and oxide scale spallation, as indicated by Stott et al. [37] and Marasco and Young [33].

The present study shows that Si is found predominately underneath the Cr-rich oxide scale. Before the oxide nodules formed, distinct silica particles (Figs. 5 and 9) are formed along and

accumulated at the oxide/metal interface. Si hardly diffuses in iron oxides (Figs.6, 7 and 10). Less Si existing at the metal-scale interface may result in poor adhesion (Figs. 4a and 5a). Some researchers concluded that SiO_2 formed at the metal-scale interface acts as a diffusion barrier which can reduce the rate of penetration of oxygen and pegs the chromia scale on the substrate [38-39]. Also, SiO_2 at the metal-scale interface can decrease the activity of iron at the interface, therefore it can prevent the formation of iron-rich oxides [34]. Our study shows that the silica layer is porous and some pores might become the initial sites for the formation of big cavities at the metal-oxide scale interface with the progress of time.

Fig. 14 shows the cross section of the Cr_2O_3 scale with defects and the evolution of the oxide nodules on the samples at the temperature that the breakaway oxidation is induced. Fig. 14a and b are the cross section of oxide nodules formed on B443NT at the temperature of 1090 °C. Fig. 14c and d are the cross sections of the oxide scale formed on B445J1M at the temperature of 1150 °C. For both stainless steels, it can be seen that the internal Fe-Cr spinel is developed before the outside iron oxides form. Before Cr_2O_3 scale fails, the defects at the metal-scale interface, e.g. pores, start to grow. Some parts of the Cr_2O_3 scale have detachment from the substrate, as shown in Fig. 14c and d. In the case of B443NT, influence of Cr volatilisation under wet air would cause Cr depletion in the steel subscale; therefore internal oxidation of Cr is easily occurred, as shown in Fig. 14b. The breakaway mechanism can be explained by the evaporation of chromium volatile species [11-12] and the enhanced internal oxidation in steam [40-42]. In the case of the steel B445J1M, influence of Cr volatilisation under wet air is not so significant, because Mr-Cr spinel layer is present at the external gas-oxide interface (Fig. 13b) and reduces Cr volatilisation. However, the detachment or pores at the metal-scale interface and cracks in the Cr_2O_3 scale are obvious. The breakaway mechanism can be explained by the mechanically induced chemical failure [24] or hydrogen/water dissociation mechanism as water dissociation is endothermic at high temperature [43-44]. Rapid internal

precipitation of nonprotective oxides such as $(Fe,Cr)_3O_4$ form in the Cr-depleted zone. The mobility of Fe ions in Fe-Cr spinel is higher than that of Cr ions, allowing Fe ions to migrate outwards through Fe-Cr spinel and react with O_2 to form outer iron oxides. On the other hand, the formation of Fe-Cr spinel is mainly controlled by the inward diffusion of oxygen. From our study, the mechanism of the development of such an oxide nodule can be illustrated in Fig. 15. Fig. 15a shows that voids are left at the metal-scale interface due to Fe ions diffuse outwards quickly from Cr-depletion subscale and the oxide nodule grows fast. Fig. 15b shows that Cr_2O_3 scale is regenerated underneath the Fe-Cr spinel if the Cr in the subscale is replenished and the concentration of Cr reaches the condition to form continuous Cr_2O_3, and this has been explained in the discussion. The formation of the regenerated Cr_2O_3 can be a good diffusion barrier, suppressing Fe to diffuse outwards and O to diffuse inwards. Therefore, the oxide growth rate is declined, and usually this kind of oxide nodules display better adhesion without pores at the metal-scale interface (Fig. 11b). Fig. 15c and d shows the cycling phenomenon of the breakdown of the Cr_2O_3 scale. The wider range of the Cr depletion in the subscale, and the faster the oxide growth rate will lead to more voids at the metal-scale interface (Fig. 11a).

At the initial stage of breakaway oxidation for both the stainless steels, the localised oxide nodules form randomly at different holding times. With the progress of time, the localised oxide nodules will merge until all surfaces are covered with iron oxides (Fig. 4d). The surfaces appear coarse and the metal-scale interface appears convoluted because the oxide nodules do not appear and grow simultaneously at the same speed. In the case of B443NT, due to its high oxide growth rate after breakaway oxidation, the oxide nodules form and spread quickly, and at the end of test time, a thicker oxide scale will be formed.

5. Conclusions

The isothermal oxidation behaviours of ferritic stainless steel grades B443NT and B445J1M were studied at temperatures from 1000 to 1150 °C in simulated reheating atmosphere containing 18% water vapour.

Before breakaway oxidation occurs, the formation of Cr-rich oxide follows a parabolic law with time. Breakaway oxidation occurs at 1090 °C for B443NT, which is 60 °C lower than that for B445J1M.

The formation of localised iron oxide nodules marks the onset of breakaway oxidation. However two stainless steels present different breakaway oxidation phenomena. The rate of oxidation is accelerated abruptly for B443NT but not so significant for B445J1M. Mn diffuses in the substrate and the Cr_2O_3 scale very quickly at the high temperature. The formation of compact and continuous spinel $(Mn,Cr)_3O_4$ at the gas/scale interface on B445J1M can reduce $CrO_2(OH)_2$ volatilisation in humid atmosphere.

Localised oxides were formed and merged with the progress of time. The surface with localised oxide nodules is coarse and the metal-scale interface is convoluted. The oxide nodules with the regenerated Cr_2O_3 at the metal-scale interface exhibit better adhesion without displaying pores or cavities.

The thick and comparable uniform oxide scale can be achieved at reheating temperature 1150 °C for the steel B443NT.

Acknowledgements

The authors acknowledge the Baosteel-Australian Joint Centre financial support for the current study. We would like to also acknowledge Baosteel, China for providing the materials used in this investigation. Also we are very grateful to the anonymous reviewers for their

insightful suggestions.

References

[1] M. Cortie, Ferritic Stainless Steels, in: Encyclopedia of Materials: Science and Technology (Second ed.), Elsevier, Oxford, 2001, pp. 3037-3039.

[2] W. Jin, J.-Y. Choi, Y.-Y. Lee, ISIJ Int., 38 (1998) 739-743.

[3] S.R.J. Saunders, M. Monteiro, F. Rizzo, Prog. Mater Sci., 53 (2008) 775-837.

[4] H. Buscail, S. Heinze, P. Dufour, J.P. Larpin, Oxid. Met., 47 (1997) 445-464.

[5] H. Buscail, R. Rolland, C. Issartel, F. Rabaste, F. Riffard, L. Aranda, M. Vilasi, J Mater Sci, 46 (2011) 5903-5915.

[6] E. Essuman, G.H. Meier, J. Zurek, M. Hansel, Oxid Met, 69 (2008) 143-162.

[7] A. Agüero, V. González, M. Gutiérrez, R. Muelas, Surf. Coat. Technol., 237 (2013) 30-38.

[8] D.L. Douglass, P. Kofstad, P. Rahmel, G.C. Wood, Oxid. Met., 45 (1996) 529-620.

[9] H.C. Graham, H.H. Davis, J. Am. Ceram. Soc., 54 (1971) 89-93.

[10] A. Yamauchi, K. Kurokawa, H. Takahashi, Oxid. Met., 59 (2003) 517-527.

[11] X. Peng, J. Yan, Y. Zhou, F. Wang, Acta Mater., 53 (2005) 5079-5088.

[12] H. Asteman, J.E. Svensson, L.G. Johansson, Oxid. Met., 57 (2002) 193-216.

[13] J.E. Hammer, S.J. Laney, R.W. Jackson, K. Coyne, F.S. Pettit, G.H. Meier, Oxid. Met., 67 (2007) 1-38.

[14] M. Palcut, L. Mikkelsen, K. Neufeld, M. Chen, R. Knibbe, P.V. Hendriksen, Corros. Sci., 52 (2010) 3309-3320.

[15] Z.Y. Chen, L.J. Wang, F.S. Li, K.C. Chou, J. Alloys Comp., 574 (2013) 437-442.

[16] D.J. Young, High Temperature Oxidation And Corrosion Of Metals, Elsevier, 2008.

[17] A.M. Huntz, J. Mater. Sci. Lett., 18 (1999) 1981-1984.

[18] Z. Yang, G. Xia, P. Singh, J.W. Stevenson, Solid State Ionics, 176 (2005) 1495-1503.

[19] A. Rahmel, Mater. Corros., 39 (1988) 354-354.

[20] P. Moulin, A.M. Huntz, P. Lacombe, Acta Metall., 28 (1980) 745-756.

[21] A.M. Huntz, A. Reckmann, C. Haut, C. Severac, M. Herbst, F.C.T. Resende, A.C.S. Sabioni, Mater. Sci. Eng. A, 447 (2007) 266-276.

[22] W. Pavlichko, J.H. Hoke, Microstructural Science, Vol. 4. American Elsevier Publishing Co. Inc., New York, Oxford, Amsterdam. 1976, 3-12, (1976).

[23] S. Henry, A. Galerie, L. Antoni, Mater. Sci. Forum, 369-372 (2001) 353-360.

[24] H.E. Evans, Oxid. Met., 52 (1999) 379-401.

[25] C. Wagner, J. Electrochem. Soc., 99 (1952) 369.

[26] N.K. Othman, N. Othman, J. Zhang, D.J. Young, Corros. Sci., 51 (2009) 3039-3049.

[27] M. Schütze, D. Renusch, M. Schorr, Mater. High Temp., 22 (2005) 113-120.

[28] B. Pujilaksono, T. Jonsson, H. Heidari, M. Halvarsson, J.-E. Svensson, L.-G. Johansson, Oxid. Met, 75 (2011) 183-207.

[29] D.J. Young, B.A. Pint, Oxid. Met., 66 (2006) 137-153.

[30] E.J. Opila, D.L. Myers, N.S. Jacobson, I.M. Nielsen, D.F. Johnson, J.K. Olminsky, M.D. Allendorf, J. Phys. Chem. A, 111 (2007) 1971-1980.

[31] G.R. Holcomb, D.E. Alman, Scripta Mater., 54 (2006) 1821-1825.

[32] M. Reichardt, Wire Ind., 68 (2001) 503, 505-507.

[33] A.L. Marasco, D.J. Young, Oxid. Met., 36 (1991) 157-174.

[34] S. Rao, Oxid. Met., 77 (2011) 9-15.

[35] A.C.S. Sabioni, A.M. Huntz, L.C. Borges, F. Jomard, Philos. Mag., 87 (2007) 1921-1937.

[36] C. Issartel, H. Buscail, Y. Wang, R. Rolland, M. Vilasi, L. Aranda, Oxid Met, 76 (2011) 127-147.

[37] F.H. Stott, F.I. Wei, C.A. Enahoro, Mater. Corros., 40 (1989) 198-205.

[38] R. Pettersson, L. Liu, J. Sund, Corros. Eng. Sci. Techn., 40 (2005) 211-216.

[39] R.N. Durham, B. Gleeson, D.J. Young, Oxid. Met., 50 (1998) 139-165.

[40] E. Essuman, G.H. Meier, J. Żurek, M. Hänsel, L. Singheiser, W.J. Quadakkers, Scripta Mater., 57 (2007) 845-848.

[41] E. Essuman, G.H. Meier, J. Żurek, M. Hänsel, W.J. Quadakkers, Oxid. Met., 69 (2008) 143-162.

[42] M. Ani, A. Mohd Hanafi Bin, K. Toshiya, U. Mitsutoshi, K. Kenichi, Mater. Trans., JIM, 50 (2009) 2656.

[43] S.-Y. Cheng, S.-L. Kuan, W.-T. Tsai, Corros. Sci., 48 (2006) 634-649.

[44] A. Galerie, S. Henry, Y. Wouters, M. Mermoux, J.-P. Petit, L. Antoni, Mater. High Temp., 22 (2005) 105-112.

Table Captions:

Table 1 Chemical compositions of the ferritic stainless steels (wt.%).

Table 2 Values of K_p obtained between 1000 and 1150 °C for the B445J1M steel oxidised in humid atmosphere containing 18% water vapour.

Figure Captions:

Fig. 1. Schematic diagram of the experimental apparatus.

Fig. 2. Mass change versus time curves for the (a) B443NT and (b) B445J1M steels oxidised for 120 min at different temperatures in humid atmosphere containing 18% water vapour.

Fig. 3. XRD patterns of the oxide scales formed on the (a) B443NT and (b) B445J1M steels after oxidation at different temperatures in humid atmosphere containing 18% water vapour.

Fig. 4. Surface morphologies of the B443NT steel oxidised in humid atmosphere containing 18% water vapour: (a) 1000 °C (b) 1030 °C (c) 1090 °C, and (d) 1150 °C.

Fig. 5. Cross sections and EDS line scanning element analysis of the B443NT steel oxidised in humid atmosphere containing 18% water vapour: (a) 1000°C, and (b) 1030 °C and (c) 1060 °C.

Fig. 6. Element maps of the cross section of the B443NT steel oxidised at 1090 °C in humid atmosphere containing 18% water vapour.

Fig. 7. EDS element maps of the cross section of B443NT steel oxidised at 1150 °C in humid atmosphere containing 18% water vapour.

Fig. 8. Surface morphologies (a-d) and profiles (e,f) of the B445J1M steel oxidised in humid atmosphere containing 18% water vapour: (a) 1000 °C, (b) 1090 °C, (c,e) 1120 °C, and (d,f) 1150 °C.

Fig. 9. Cross sections and EDS line scanning element analysis of the B445J1M steel oxidised in humid atmosphere containing 18% water vapour: (a) 1030°C, (b) 1060 °C (c) 1090 °C and (d) 1120 °C.

Fig. 10. EDS element maps of the cross section of the B445J1M steel oxidised at 1150 °C in humid atmosphere containing 18% water vapour.

Fig. 11. The cross section and EDS line element analysis of the metal-oxide interface of the oxide nodule formed on the two stainless steels oxidised in humid atmosphere containing 18% water vapour at 1150 °C: (a) B443NT, and (b) B445J1M.

Fig.12. (a) Arrhenius plot of oxidation parabolic constants for B445J1M, and ((b) Parabolic plot of graph of breakaway oxidation of mass gain against square root oxidation time at 1150 °C for the two stainless steels.

Fig.13. Cross section of the chromia scale formed at 1150 °C in humid atmosphere containing 18% water vapour at 1150 °C: (a) B443NT, and (b) B445J1M.

Fig. 14. Cross sections of the metal-scale interface on the two stainless steels oxidised in humid atmosphere containing 18% water vapour: (a,b) oxide nodule formed at 1090 °C on B443NT, and (c,d) Oxide scale defects and oxide nodule formed at 1150 °C on B445J1M.

Fig. 15. Schematic illustration showing the development of oxide nodule growth.

Table 1 Chemical compositions of the ferritic stainless steels (wt.%).

	C	Si	Mn	P	Cr	Cu	Mo	Ti	Nb
B445J1M	≤0.01	0.30	0.15	0.03	21.50	0.10	0.60	≤0.20	0.12
B443NT	≤0.01	0.35	<0.10	0.00	21.00	0.40	0.00	0.14	0.20

Table 2 Values of K_p obtained between 1000 and 1150 °C for B445J1M steels oxidised in humid atmosphere containing 18% water vapour.

Temperature (°C)	K_p values ($mg^2 \cdot cm^{-4} \cdot s^{-1}$)	R^2
1000	3.5×10^{-4}	0.72
1030	2.1×10^{-4}	0.87
1060	3.3×10^{-4}	0.89
1090	5.4×10^{-4}	0.93
1120	1.0×10^{-3}	0.95
1150 (before 10 min)	8.6×10^{-3}	0.94
1150 (after 10 min)	3.0×10^{-3}	0.97

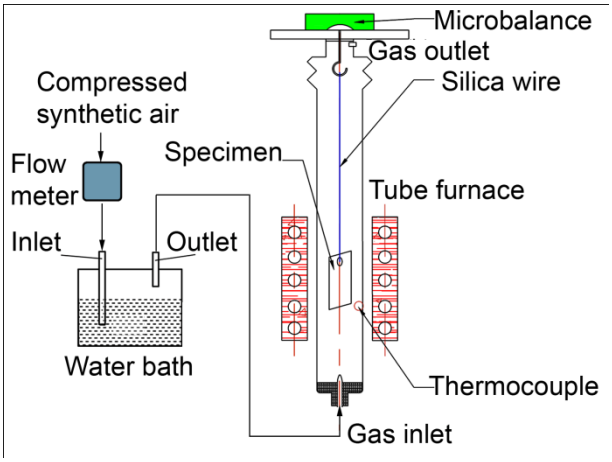

Fig. 1. Schematic diagram of the experimental apparatus.

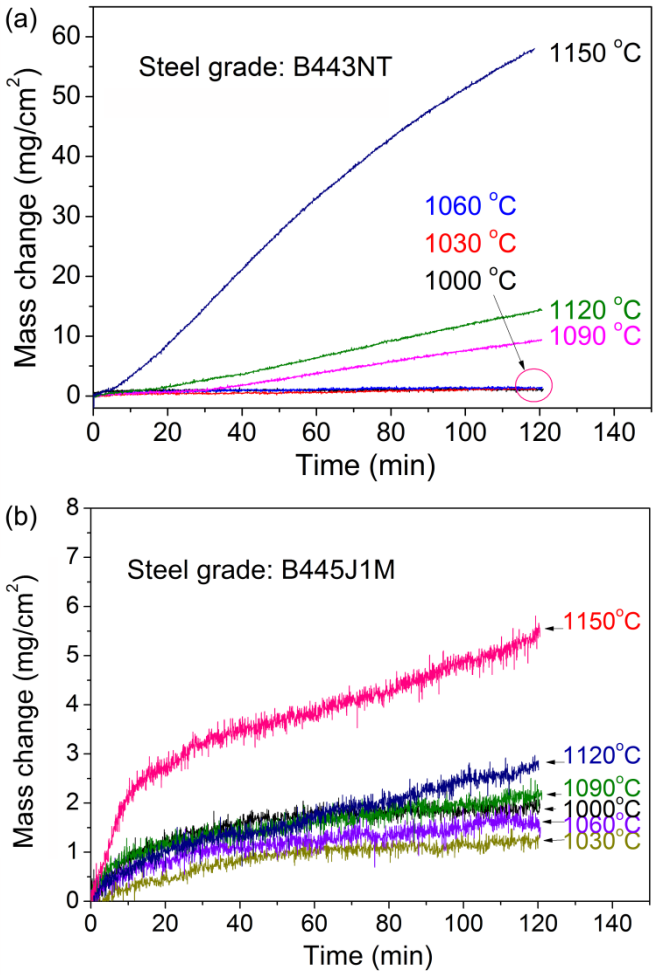

Fig. 2. Mass change versus time curves for the (a) B443NT and (b) B445J1M steels oxidised for 120 min at different temperatures in humid atmosphere containing 18% water vapour.

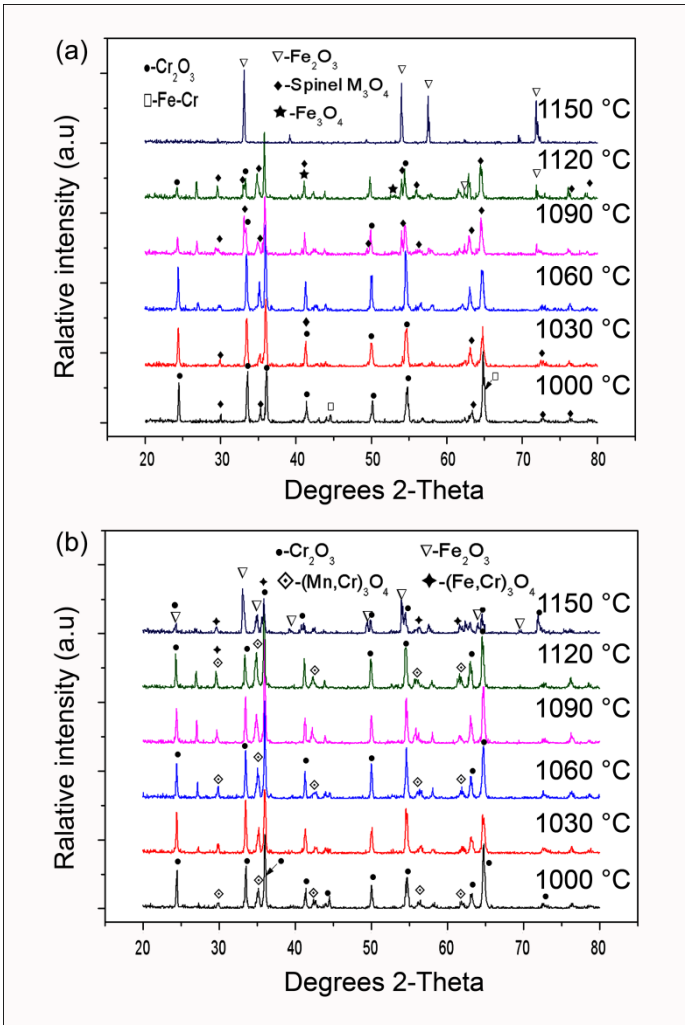

Fig. 3. XRD patterns of the oxide scales formed on the (a) B443NT and (b) B445J1M steels after oxidation at different temperatures in humid atmosphere containing 18% water vapour.

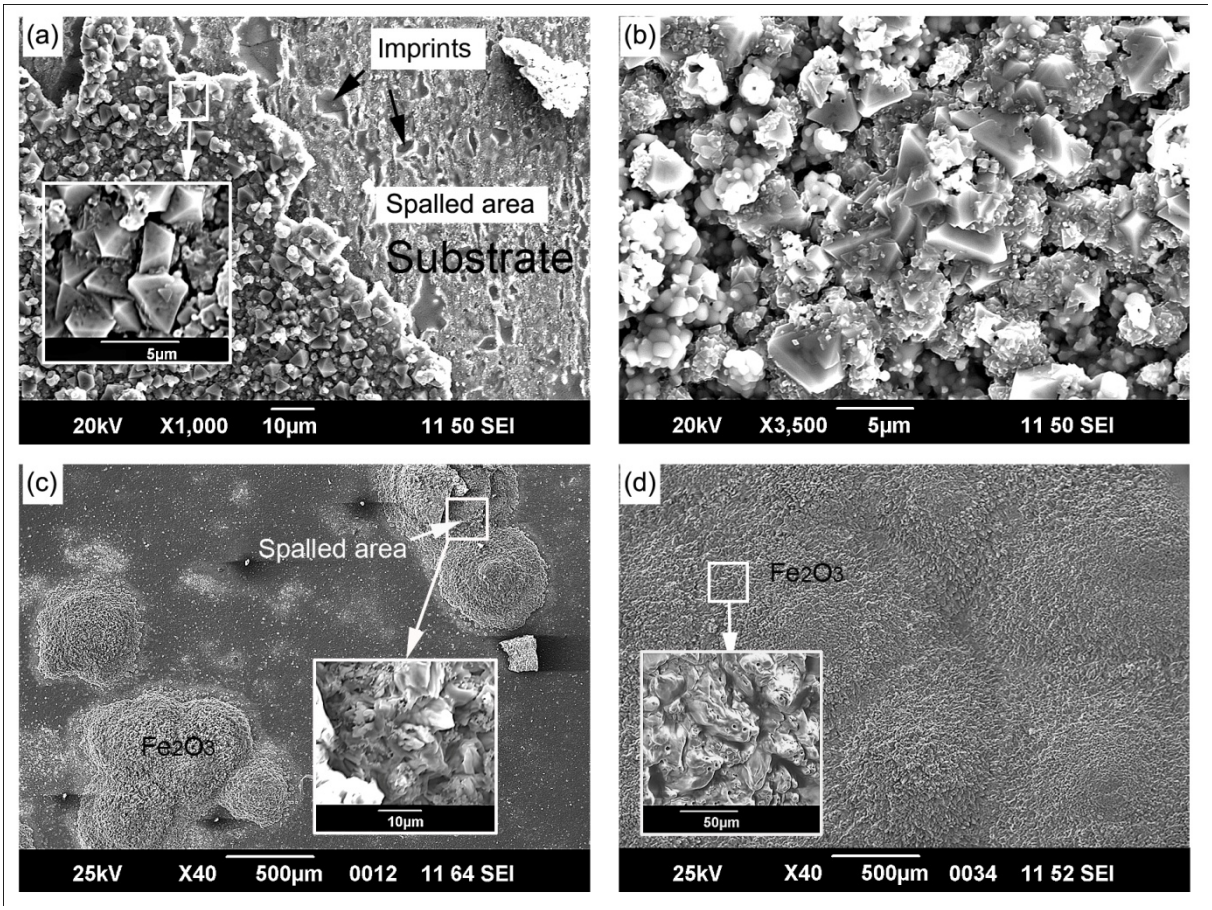

Fig. 4. Surface morphologies of the B443NT steel oxidised in humid atmosphere containing 18% water vapour: (a) 1000 °C (b) 1030 °C (c) 1090 °C, and (d) 1150 °C.

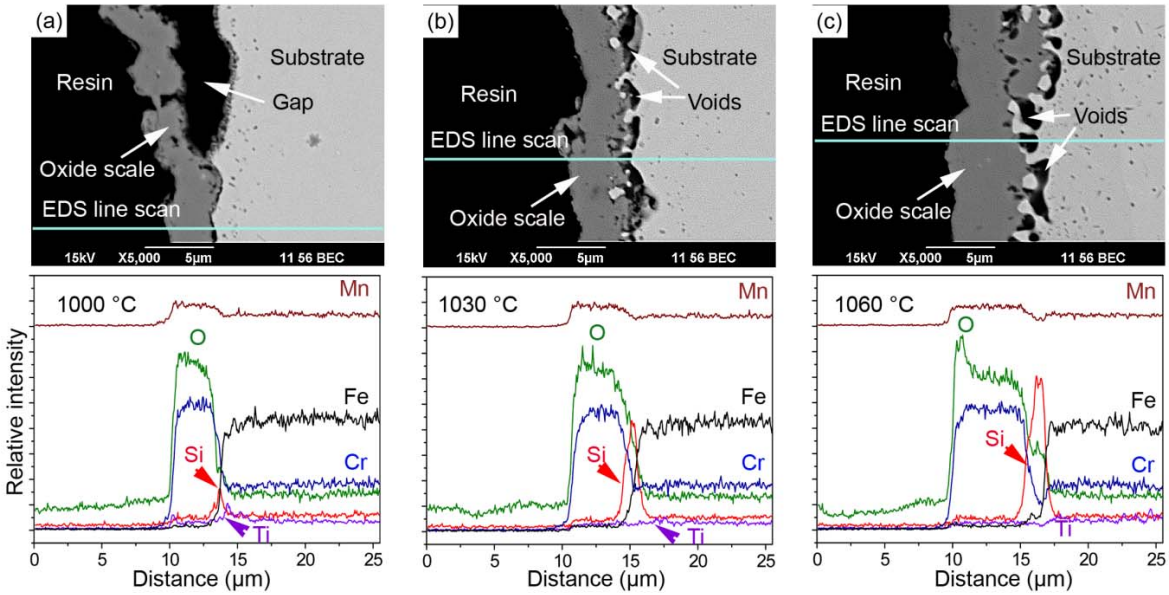

Fig. 5. Cross sections and EDS line scanning element analysis of the B443NT steel oxidised in humid atmosphere containing 18% water vapour: (a) 1000°C, and (b) 1030 °C and (c) 1060 °C.

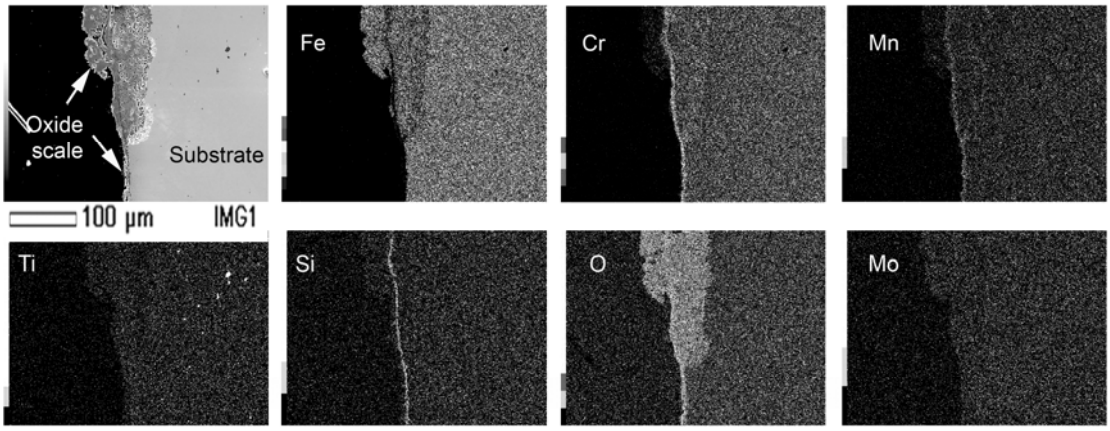

Fig. 6. Element maps of the cross section of the B443NT steel oxidised at 1090 °C in humid atmosphere containing 18% water vapour.

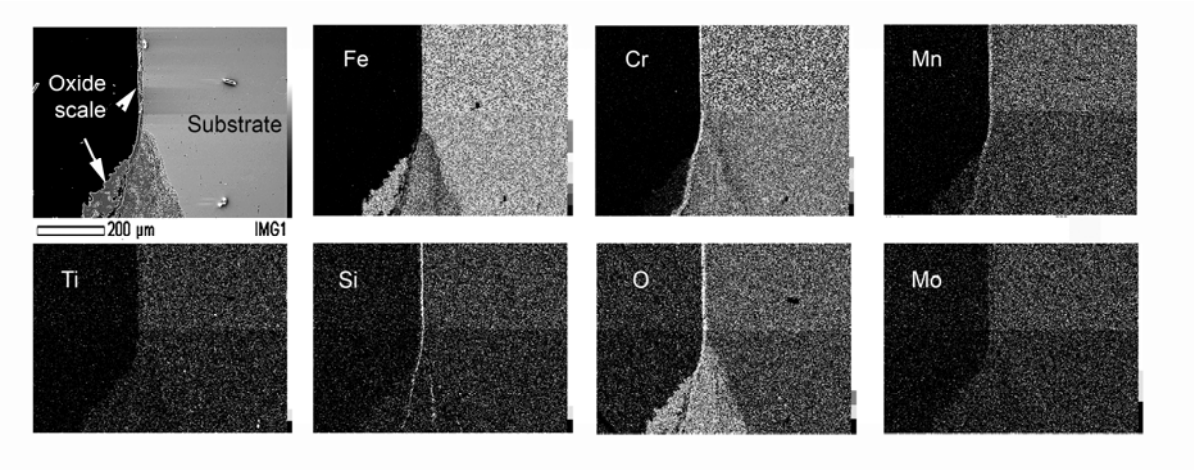

Fig. 7. EDS element maps of the cross section of B443NT steel oxidised at 1150 °C in humid atmosphere containing 18% water vapour.

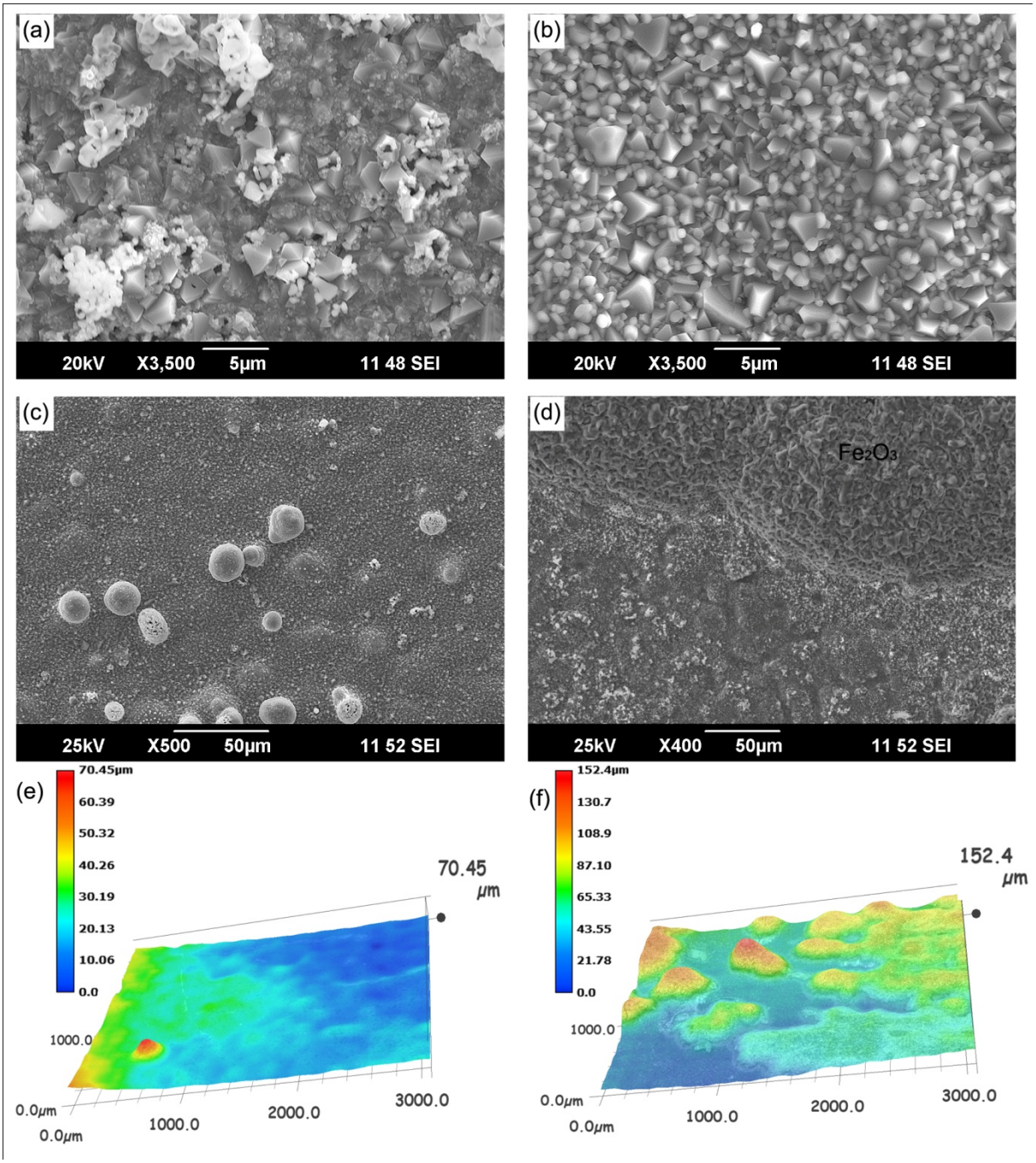

Fig. 8. Surface morphologies (a-d) and profiles (e,f) of the B445J1M steel oxidised in humid atmosphere containing 18% water vapour: (a) 1000 °C, (b) 1090 °C, (c,e) 1120 °C, and (d,f) 1150 °C.

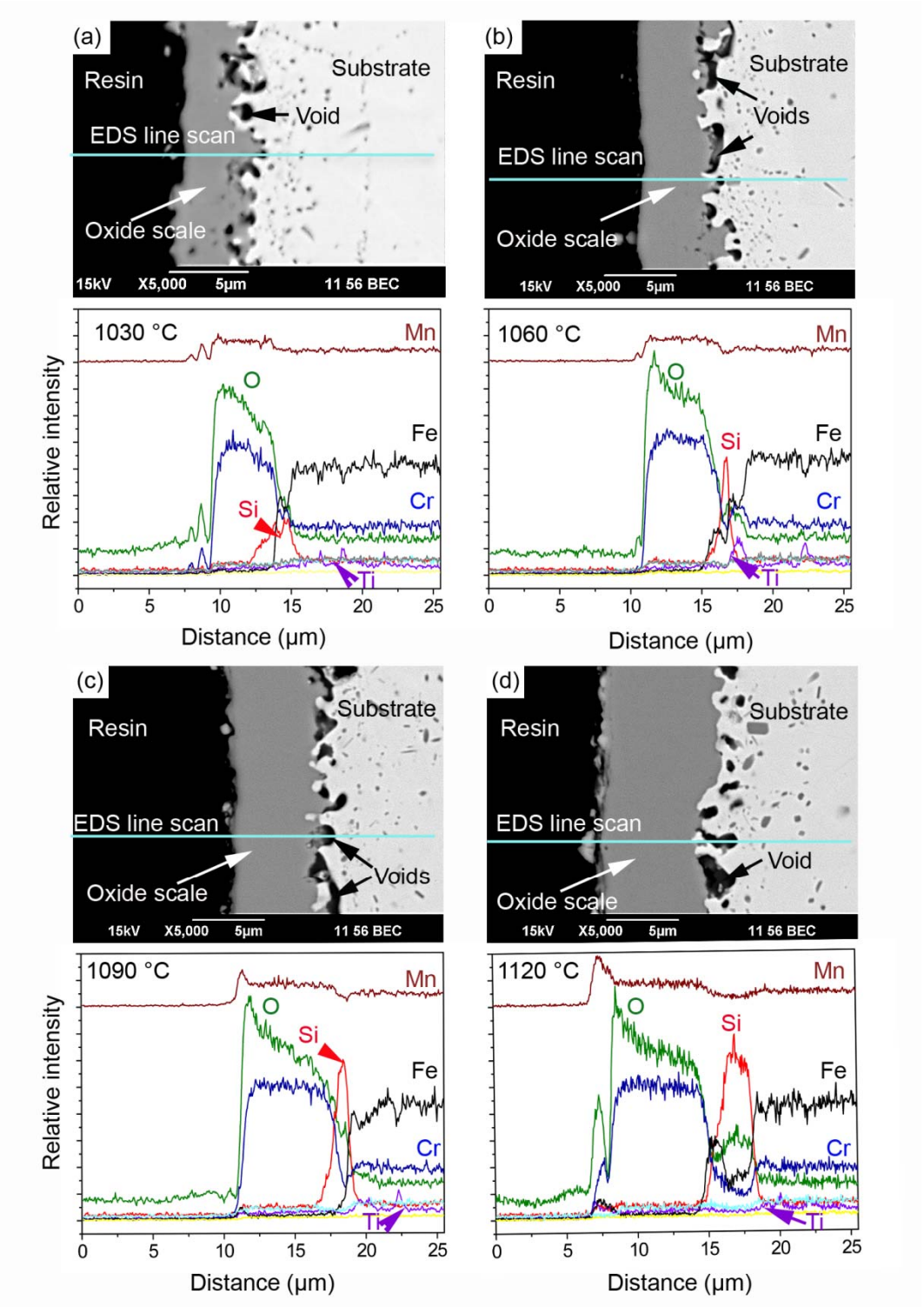

Fig. 9. Cross sections and EDS line scanning element analysis of the B443NT steel oxidised in humid atmosphere containing 18% water vapour: (a) 1030°C, (b) 1060 °C (c) 1090 °C and (d) 1120 °C.

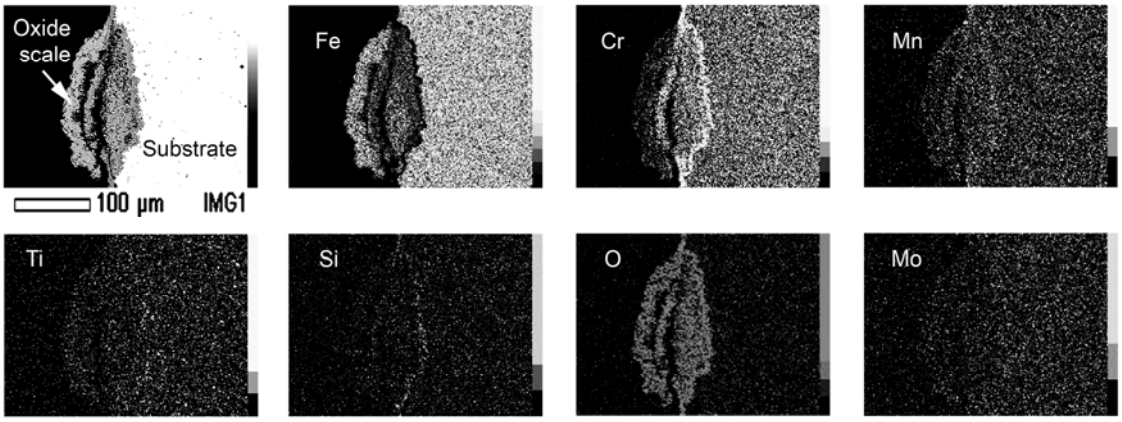

Fig. 10. EDS element maps of the cross section of the B445J1M steel oxidised at 1150 °C in humid atmosphere containing 18% water vapour.

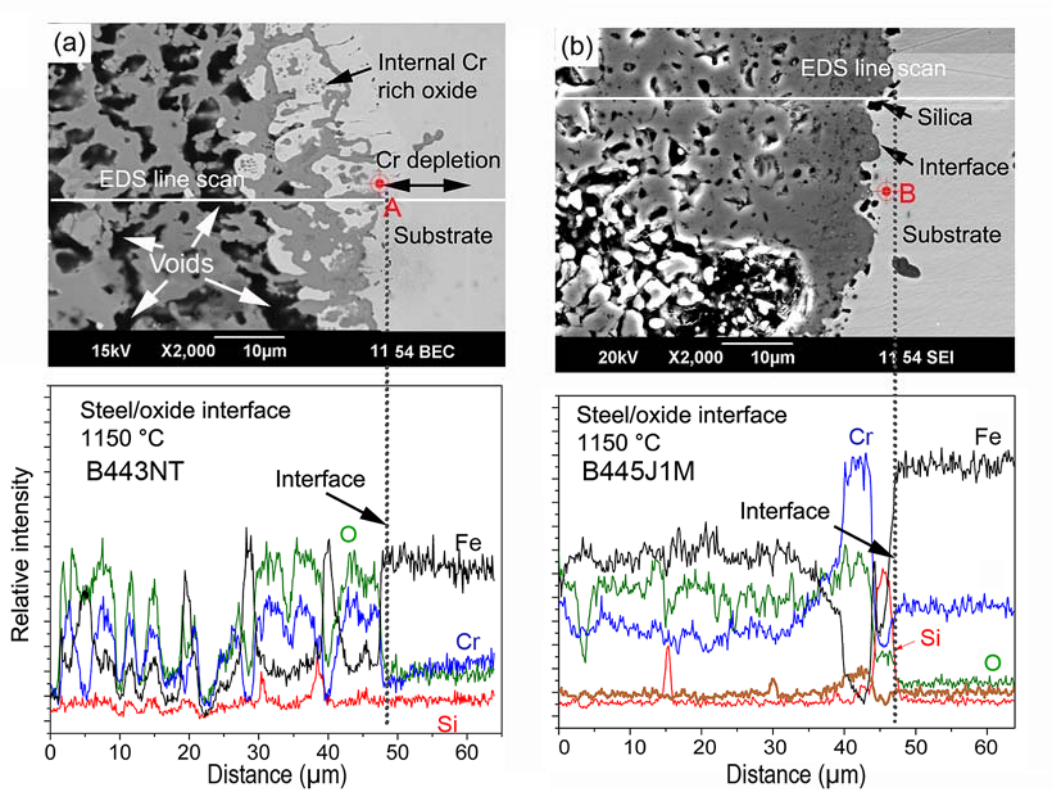

Fig. 11. The cross section and EDS line element analysis of the metal-oxide interface of the oxide nodule formed on the two stainless steels oxidised in humid atmosphere containing 18% water vapour at 1150 °C: (a) B443NT, and (b) B445J1M.

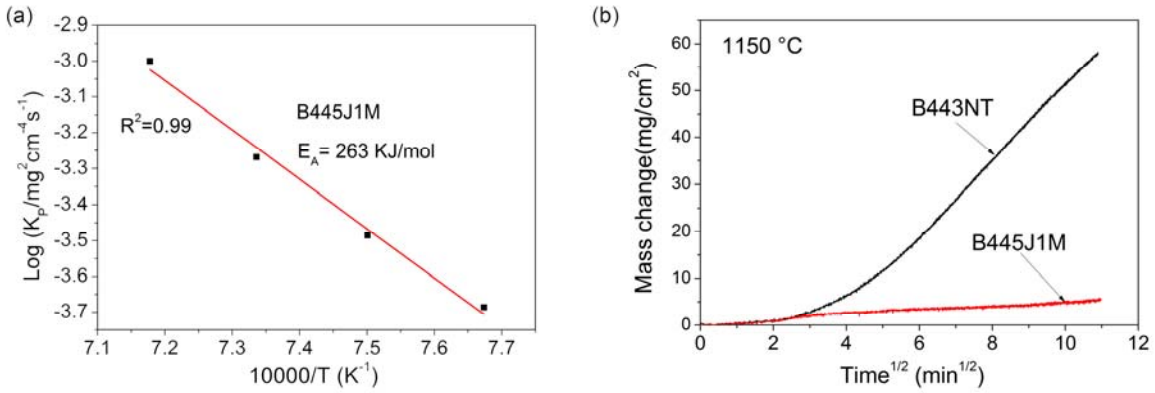

Fig.12. (a) Arrhenius plot of oxidation parabolic constants for B445J1M, and (b) Parabolic plot of graph of breakaway oxidation of mass gain against square root oxidation time at 1150 °C for the two stainless steels.

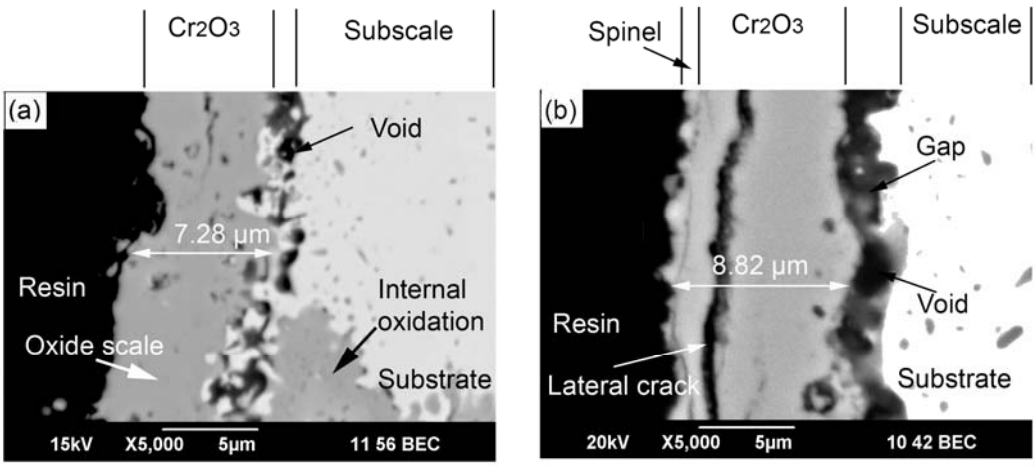

Fig.13. Cross section of the chromia scale formed at 1150 °C in humid atmosphere containing 18% water vapour at 1150 °C: (a) B443NT, and (b) B445J1M.

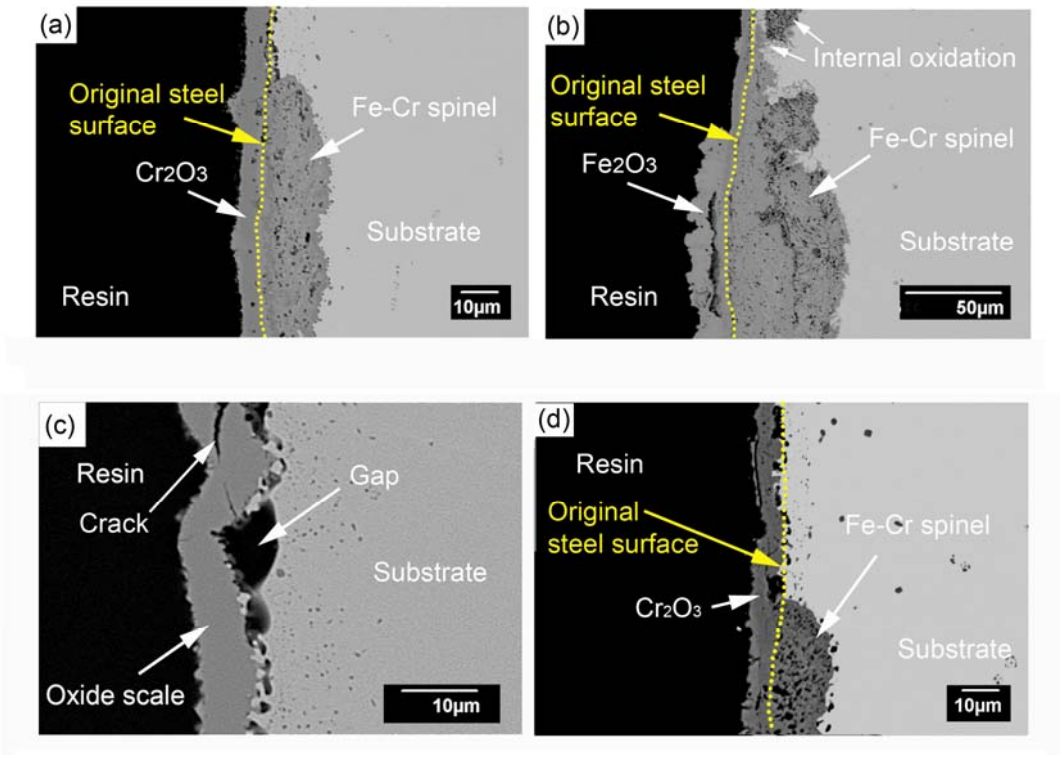

Fig. 14. Cross sections of the metal-scale interface on the two stainless steels oxidised in humid atmosphere containing 18% water vapour: (a,b) oxide nodule formed at 1090 °C on B443NT, and (c,d) Oxide scale defects and oxide nodule formed at 1150 °C on B445J1M.

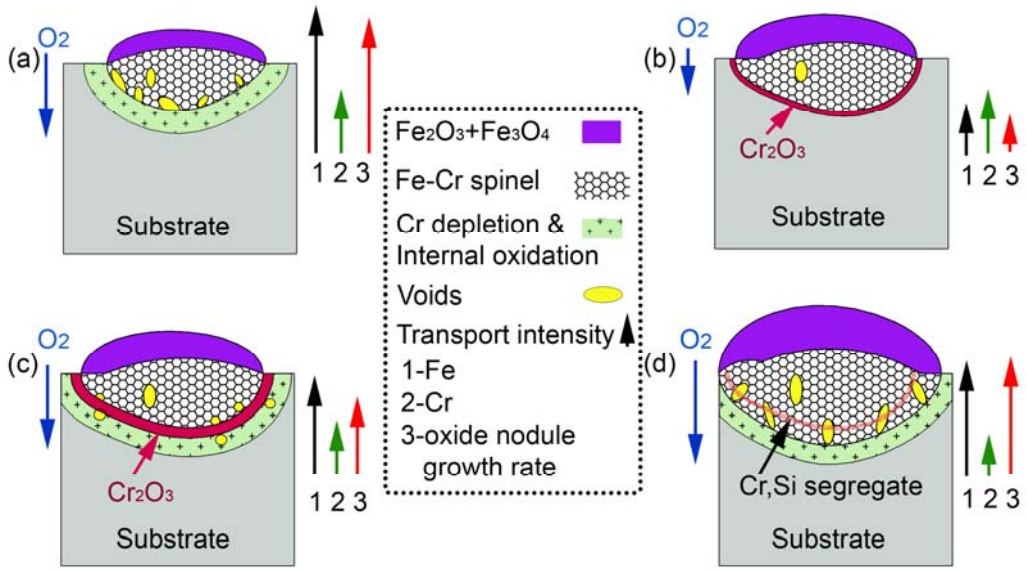

Fig. 15. Schematic illustration showing the development of oxide nodule growth.